# Application of Frictional Contact in Geotechnical Engineering

Daichao Sheng[1]; Peter Wriggers[2]; and Scott W. Sloan[3]

**Abstract:** Soil-structure interaction is traditionally simplified to prescribed boundary conditions or modeled by joint elements. Both of these approaches are limited to small and continuous relative displacements at the interface. The use of contact constraints opens up a fresh range of possibilities for geotechnical analysis, especially for cases involving large interfacial deformation. This paper demonstrates the application of computational contact mechanics in geotechnical engineering. It first outlines a general description of kinematic constraints for frictional contact and the associated numerical algorithms. A number of classical geotechnical problems are then analyzed using finite-element contact methods. These problems include a strip footing under eccentric and inclined loads and a cone penetration test. It is shown that the finite-element method with frictional contact is indeed very useful in geotechnical analysis, and can provide solutions to problems that are otherwise very difficult to analyze.

**DOI:** 10.1061/(ASCE)1532-3641(2007)7:3(176)

**CE Database subject headings:** Soil-structure interaction; Finite element method; Interfaces; Contacts; Geotechnical engineering; Friction.

## Introduction

In geotechnical engineering, loads are transferred between structures and soils principally through contact of surfaces. Such loading conditions are traditionally simplified either as prescribed loads (by assuming complete flexibility of the structure) or as prescribed displacements (by assuming complete rigidity of the structure). These crude simplifications often lead to inaccurate predictions of the real behavior, and are only possible when the surfaces in contact are known a priori. Contacts between soils and structures in many cases involve large frictional sliding as well as surface separation and reclosure, are highly variable during the loading procedure, and cannot be modeled by simple prescribed boundary conditions. They can dramatically affect the overall load capacity of a structure. Examples where frictional contact is important include structural foundations under eccentric loading, pile foundations, soil anchors, retaining walls, geotextile reinforcements in embankments and retaining structures, and soil testing devices that are pushed into the ground to measure material properties.

In addition to the use of simple prescribed boundary conditions, soil–structure interaction is traditionally modeled by joint elements. These elements, initially developed for rock joints, typically use normal and tangential stiffness to model the pressure transfer and friction at the interface (Goodman et al. 1968; Desai et al. 1984; Wilson 1992). They are very flexible for modeling interfacial behavior such as dilation and shear strength softening. They can have a small or even zero thickness, but otherwise are not much different to other continuum elements. Because they are predefined and their topology remains unchanged during the solution procedure, they are only suitable for predefined interfaces with small interfacial deformation. One notable exception to this rule, however, has been described by Van den Berg (1994), who combined interface elements with an Eulerian formulation of large deformation to simulate a soil mass streaming past a fixed cone. Such a method, although novel, is limited to cases where the material flows at boundaries are known, which is rarely true in reality. In addition, the method of Van den Berg cannot simulate a penetration procedure which starts from the ground surface. More recently, Liyanapathiranna et al. (2000) presented a new method for modeling large deformations associated with installation of displacement piles. By successively activating predefined pile–soil interface and pile elements, they were able to model large penetration of open-ended piles with negligible wall thickness. Because the inactive pile and interface elements must be predefined, they cannot occupy space when they are inactive. Therefore, it is difficult to extend their method to closed-ended piles or open-ended piles with significant wall thickness.

The first application of frictional contact to model soil–structure interaction is probably due to Katona (1983), where a finite-element formulation based on node-to-node contact and the Lagrangian multiplier method is presented and used to simulate the interaction between a buried culvert and the surrounding soil. Although the method by Katona (1983) was able to handle difficulties like surface separation and reclosure, the node-to-node contact formulation used in his study is limited to geometrically linear problems that involve only small relative sliding between the contacting nodes. Mabsout et al. (1995) used the slide-line frictional contact method to model pile penetration in undrained, normally consolidated clays. They were able to model pile pen-

[1]Associate Professor, School of Engineering, The Univ. of Newcastle, NSW 2308, Australia.

[2]Professor, Institut fuer Baumechanik und Numerische Mechanik, Univ. of Hannover, Germany.

[3]Professor, School of Engineering, The Univ. of Newcastle, NSW 2308, Australia.

Note. Discussion open until November 1, 2007. Separate discussions must be submitted for individual papers. To extend the closing date by one month, a written request must be filed with the ASCE Managing Editor. The manuscript for this paper was submitted for review and possible publication on May 26, 2005; approved on September 12, 2006. This paper is part of the ***International Journal of Geomechanics***, Vol. 7, No. 3, June 1, 2007. ©ASCE, ISSN 1532-3641/2007/3-176–185/$25.00.

etration to a finite depth and, hence, predict a number of important features, including total and shaft resistances of the pile and excess pore pressure development in the soil. However, their method is also limited to small scale sliding and can only model piles in prebored holes.

Because of its practical importance and complexity, nonlinear contact mechanics, which deals with the contact kinematics of solid bodies, is a very active research area in computational mechanics. In particular, contact problems involving rigid, elastic and simple elastoplastic solid bodies have attracted considerable attention over the last two decades. Even though significant advances have been made in designing algorithms for solving contact problems, merely achieving convergence can be very difficult under many circumstances (Christensen et al. 1998; Pietrzak and Curnier 1999; Barber and Ciavarella 2000; Wriggers 2002; Liu et al. 2003). This is especially true for contact problems in soils, where the constitutive models are usually complex.

This paper first outlines a general finite-element formulation of contact kinematics and contact constraints for geotechnical problems. The associated solution algorithms at different levels are also discussed. To demonstrate the use of the contact constraints, a number of common geotechnical problems are then analyzed.

## Formulation of Contact Kinematics

### Principle of Virtual Work

The basis of the finite-element method is the principle of virtual work. Without contact, this principle states that if $\delta\mathbf{u}$ are virtual displacement fields satisfying the displacement boundary conditions, then equilibrium is satisfied provided:

$$\int_V \delta\boldsymbol{\epsilon}^T\boldsymbol{\sigma}dV + \int_V \delta\mathbf{u}^T\rho\ddot{\mathbf{u}}dV - \int_V \delta\mathbf{u}^T\mathbf{b}dV - \int_S \delta\mathbf{u}^T\mathbf{t}dS = \delta\mathbf{u}^T\mathbf{G}(\mathbf{u}) = 0 \quad (1)$$

where $\delta\boldsymbol{\epsilon}$ denotes the variation of the strains derived from the virtual displacements; $\boldsymbol{\sigma}$=stresses; $\ddot{\mathbf{u}}$=acceleration vector; $\rho$=density; $\mathbf{b}$=body force vector; $\mathbf{t}$=distributed force acting on the boundary $S$ of the volume $V$; and the operator $\mathbf{G}(\mathbf{u})$=measure of unbalanced forces. For a nonlinear problem, Eq. (1) is typically applied incrementally. For geometrically nonlinear problems, the configuration ($V$ and $S$) in Eq. (1) refers to the one at which the solution is sought. This configuration is not known and has to be transferred to a known configuration, e.g., the one at the start of the current time step [updated Lagrangian (UL)] or the one at time zero [total Lagrangian (TL)]. In either case, the second Piola–Kirchhoff stress tensor and the Green–Lagrangian strain tensor are usually used in places of the Cauchy stress tensor $\boldsymbol{\sigma}$ and Almansi strain tensor $\boldsymbol{\epsilon}$, respectively. For problems involving large-slip contact, the contact constraints are always described based the current configuration and therefore the UL method is preferable.

In the case of large deformations, both the TL and UL methods may result in a distorted mesh, leading to poor accuracy of the solution. To avoid severe mesh distortion, the mesh and the material displacements can be separated from each other, thus allowing the mesh to move independently from the material. This assumption leads to the formulation of the arbitrary Lagrangian–Eulerian (ALE) method. To solve Eq. (1) by this technique, two steps are usually carried out: an UL step followed by an Eulerian step. In the UL step, the UL method is used to solve the equilibrium equations. At the end of the UL step, the mesh may be distorted since it moves along with the material. Therefore, in the Euler step, a new mesh is generated for the deformed domain, based on the initial topology but without element distortion. All kinematic and static variables are then transferred from the old mesh to the new mesh using the relation between the material derivative and the mesh derivative. To obtain a less distorted mesh in the Eulerian step, robust mesh generation algorithms are required. A detailed review of alternative solution methods (including TL, UL, and ALE methods) for large deformations in geomechanics can be found in Nazem et al. (2006).

Although powerful, the ALE method is not used in the analyses presented in this paper because of its complexity. However, it may well be necessary to use this method in studying problems where mesh distortion significantly affects the results, such as in the simulation of inserting flat-ended piles into the ground.

### Contact Constraints and Numerical Treatment

Consider a system of solid bodies in contact. Contact kinematics state that for any admissible displacement, there is no interpenetration between the bodies, and the contact normal stress $\sigma_n$ can only be zero or compressive. The normal contact constraints can be represented as

$$g_n = 0, \text{ when } \sigma_n > 0; \quad g_n > 0, \text{ when } \sigma_n = 0; \quad g_n\sigma_n = 0 \quad (2)$$

where $g_n$=relative displacement in the normal direction (or the normal gap). Note that the previous normal contact conditions can easily be reformulated to allow a tensile contact stress for adhesive interfaces (Wriggers 2002).

For frictional contact with a Coulomb-type law, the tangential constraints can be expressed as

$$g_t = 0, \text{ when } \mu\sigma_n - |\sigma_t| > 0; \quad |g_t| > 0, \text{ when } \mu\sigma_n - |\sigma_t| = 0$$
$$g_t(\mu\sigma_n - |\sigma_t|) = 0 \quad (3)$$

where $g_t$=relative displacement in the tangential direction or the tangential gap; $\sigma_t$=tangential stress at contact; and $\mu$=coefficient of friction. The first part of Eq. (3) defines the state of stick, whereas the second part is associated with sliding. These equations can also be recast within the framework of elastoplasticity, see Wriggers (2002). In three-dimensional problems, there are two tangential directions and hence $g_t$ and $\sigma_t$ are vectors.

When solid bodies come into contact, the traction forces at the contact interface will also contribute to the virtual work and Eq. (1) becomes

$$\delta\mathbf{u}^T\mathbf{G}(\mathbf{u}) + \int_{\Gamma^c} (\sigma_n\delta g_n + \sigma_t\delta g_t)dS = 0 \quad (4)$$

where $\delta g_n$ and $\delta g_t$=virtual normal and tangential gap, respectively, which can be expressed in terms of the virtual displacements $\delta\mathbf{u}$, and $\Gamma^c$=boundary where contact takes place. Two new unknowns are introduced into the equilibrium equation and they are the contact forces $\sigma_n$ and $\sigma_t$. Depending on the numerical treatment of these forces, we have the two classical formulations: The Lagrange multiplier method and the penalty method.

In the Lagrange multiplier method, the normal stress is replaced by the so-called Lagrange multiplier $\lambda_n$. The tangential stress is replaced by the Lagrange multiplier $\lambda_t$ in the tangential direction for the stick state, but determined by a constitutive law for the slip state. The Lagrange multipliers are then solved from the enforcement of the contact constraints:

$$\int_{\Gamma^c} (\delta\lambda_n g_n + \delta\lambda_t g_t) dS = 0 \tag{5}$$

The integrations in Eqs. (4) and (5) can only be done for a known boundary $\Gamma^c$. In reality, this boundary is not known a priori as it depends on the solutions for the displacements and Lagrange multipliers. Therefore, the boundary must be assumed within the algorithm and the solution sought for Eqs. (4) and (5) must converge to the correct contact boundary.

In the penalty method, the normal and tangential tractions at contact are assumed to be proportional to the normal and tangential gap functions, respectively

$$\sigma_n = \epsilon_n g_n$$

$$\sigma_t = \begin{cases} \epsilon_t g_t & \text{for stick} \\ \mu\sigma_n & \text{for slip} \end{cases} \tag{6}$$

where $\epsilon_n$ and $\epsilon_t$=penalty parameter for normal and tangential contact, respectively. These penalty parameters should in theory be infinitely large to avoid surface penetration and elastic sliding under compressive normal contact stress, but naturally cannot be so in a numerical implementation. Therefore, a finite surface penetration may take place if a penalty method is used. Note that the Coulomb frictional law used in Eq. (6) for the slip state can be replaced by other constitutive laws. The penalty method does not introduce any extra degrees of freedom, so Eq. (5) is no longer needed.

We see that the Lagrange-multiplier method satisfies the contact constraints exactly. However, it requires solving for the contact traction forces as additional degrees of freedom. Due to the inherent instability caused by the nonsmooth contact constraints, the Lagrange-multiplier method may suffer from nonconvergence. On the other hand, the penalty method uses only displacements to approximate the contact constraints and can be easily implemented into a displacement finite-element code. However, good approximations of the contact constraints require high penalty parameters which may, in turn, lead to ill-conditioned global equations.

A newer procedure that overcomes the shortcomings of the penalty and Lagrange-multiplier methods is the so-called augmented Lagrangian method. In addition to the virtual work due to the Lagrange multipliers, the augmented Lagrangian method adds the virtual work done by the penalty forces to the equilibrium equation. The penalty forces are measures of constraint violations and hence should approach zero for a converged solution. The augmented Lagrangian method is implemented using a double loop algorithm in which the Lagrange multipliers are first held constant during the Newton iteration loop to solve for the weak form (Wriggers 2002; Sheng et al. 2006a). Within this structure, the updates of Lagrange multipliers are performed in such a way that the new equilibrated solution results in a reduction of the penalty forces, and hence a reduction of the constraint violation. Since the Lagrange multipliers are fixed during the Newton inner loop for the displacements, the augmented Lagrangian method can be considered as a displacement method, but the Lagrange multiplier ensures that its accuracy is not significantly affected by the penalty parameters. In other words, it enjoys the merits of both the penalty method and the Lagrange-multiplier method.

### Constitutive Laws for Soil-Structure Interfaces

As described earlier, the soil–structure interfaces modeled by contact constraints do not contain any physical material and thus do not need a material model for the interface. Contact is detected by the gap functions. If the normal gap $g_n$ is larger than zero, no contact occurs and nothing needs to be done. If $g_n$ is zero (or a small negative value in the penalty method), contact occurs and the tangential gap $g_t$ needs to be computed. In the latter case, the tractions at contact have to be computed as outlined above. Although any compressive normal force can be transferred at the interface, the tangential force is usually limited by the shear strength of the interface. In the discussion above, we have used the simple Coulomb friction law to define the interfacial shear strength. However, more advanced shear strength models can be incorporated into the contact formulation without difficulty.

Shear strength models used for steel–rock, concrete–soil, and steel–soil interfaces typically include a peak shear strength followed by a residual shear strength (Rowe and Pells 1980; Rowe and Armitage (1987); Ooi et al. 1987; Desai and Ma 1992; Leong and Randolph 1992). Softening from the peak to the residual shear strength is assumed to be related to the shear displacement, plastic shear displacement, or plastic strain. To take into account the phenomenon of peak shear strength, the Coulomb friction law may be modified to use two friction coefficients, one for static friction (peak) and one for dynamic friction (residual), as is done in some commercial finite-element codes. When the tangential traction forces at contact are smaller than the static friction strength, the relative tangential slip is zero, and the tangential Lagrange multiplier corresponds to a reaction. Once relative tangential slip occurs, the friction of the interface reduces to the dynamic value. However, such a dual-valued friction model is prone to numerical instability and is not recommended.

A further modification to this peak-residual strength model is to smooth the degradation from the peak strength to the residual strength. This degradation can be assumed to be a function of the plastic shear displacement, as in the model of Ooi et al. (1987), or a function of the shear displacement and wear as in the model of Leong and Randolph (1992). Such a smoothed softening model has the advantage that it can be handled in the same manner as an elastoplastic model.

One confusing point about different interface modeling approaches is the stiffness parameters and the dilation at interfaces. In classical joint elements, elastic normal and shear stiffnesses at the interface have to be defined. Such stiffness parameters are not required in contact constraints. However, in the penalty method as outlined above, the use of a finite penalty parameter will result in some elastic material overlap (negative normal gap) or elastic sliding (tangential gap) under compressive normal stresses. Therefore, they act like a kind of stiffness. The penalty parameters significantly affect the magnitudes of the elastic gaps, but not significantly the stresses at contact as long as these parameters are sufficiently large. Under tensile normal stresses, the "stiffnesses" in contact formulations are not required. In the Lagrange multiplier method, the contact constraints are satisfied exactly and no stiffnesses are required.

As mentioned previously, contact constraints do not contain any interfacial material and hence cannot model dilation at interfaces. Physically, dilation at soil–structure interfaces must be due to the dilation of the soil or the structure near the interface, not the interface itself. Two contacting surfaces can only open and close, which are naturally included in the contact constraints. The dilation of the soil near the interface (e.g., due to particle rotations

caused by the interfacial friction) has to be considered in the constitutive model of the soil. This feature may be regarded as a shortcoming of the contact constraint approach, even though it is physically more reasonable for soil–structure interfaces.

### Solution Methods

Certain geotechnical problems can be modeled by assuming a quasistatic state. For example, static loads applied to rate-independent dry soils or fully drained soils can be treated as being quasistatic. In such cases, the acceleration term in Eq. (1) can be dropped which, after discretization, leads to a set of nonlinear equations. These equations have to be solved incrementally along the load path.

Typical solution schemes include the Newton-Raphson and the modified Newton-Raphson iteration methods. These iterations are performed so that at the end of each load increment the unbalanced forces are reduced to a prescribed tolerance level. In contact mechanics, because the contact areas and positions at the end of a load increment are not known, the iterations should also result in the correct contact constraints. Due to the non-smooth nature of these constraints, the convergence of the Newton iterations is often very slow and highly problematic.

An alternative method for solving the governing system of nonlinear equations is to use explicit Euler methods with different orders of accuracy, e.g., the first-order accurate Euler method and the second-order accurate modified Euler method. The difference between such a pair of solutions naturally constructs a measure of the load path error, and can then be used to control the load step sizes. Abbo and Sloan (1996) and Sheng and Sloan (2001) have successfully applied such methods to solve quasistatic problems for elastoplastic soils. When applying a similar solution philosophy to problems involving contact constraints, one special issue arises with the local error measure. Traditionally, such a local error measure is only computed using degrees of freedom like displacements. If the Lagrange-multiplier method is used, the contact traction forces are degrees of freedom and can be naturally included in the local error measure, so that the error and convergence behavior of the contact constraints can be controlled directly. However, if the penalty method or the augmented Lagrangian method is used, the primary unknowns are the nodal displacements and the traditional method can be applied directly (Sheng et al. 2006b).

Once the nodal displacements are found, the strain increments within a load or time increment can be solved using the strain-displacement matrix **B** (which may be either linear or nonlinear). The stresses at the integration points are then computed by means of a stress integration scheme. The improved explicit stress integration algorithm of Sloan et al. (2001, 2002) has proven to be particularly effective for a wide range of elastoplastic soil models including critical state models and unsaturated soil models (Sheng et al. 2003). It controls the error in the computed stresses by using a local error measure to automatically subincrement the applied strain increment. The error measure is computed at each integration point by taking the difference between a first-order accurate Euler solution and a second-order accurate modified Euler solution.

Similar to elastoplastic models, advanced interface models that take into account hardening and softening behavior must be solved numerically using a stress integration model. For example, the strain hardening-softening model of Leong and Randolph (1992) can be cast in an incremental form by analogy with elastoplasticity (Wriggers 2002), and then solved using a stress integration scheme. To facilitate global convergence, the local integration scheme must be very robust and accurate. The explicit stress integration algorithm of Sloan et al. (2001, 2002) is also a good choice for integrating advanced constitutive models for soil–structure interfaces.

The numerical algorithms and constitutive models discussed earlier were all implemented in the finite-element code SNAC developed at Newcastle over the last 15 years or so. This program is presently capable of coupled and uncoupled analysis of saturated and unsaturated soils and has a number of advanced numerical algorithms that are not available in other geotechnical codes. In addition to the features mentioned previously (Sheng and Sloan 2001; Sloan et al. 2001, 2002; Sheng et al. 2002), numerical algorithms for large deformation and frictional contact have recently been developed and incorporated into this code (Nazem et al. 2006; Sheng et al. 2006b).

## Applications

For simplicity, we limit our analyses in this paper to quasistatic problems. Furthermore, we use the simple penalty method for contact treatment and the Coulomb friction law for constitutive behavior at the soil-structure interface. Unless indicated otherwise, the penalty parameters are set to $10^9$ kN/m$^3$, about 2,500 times the soil stiffness divided by the width of the soil elements beneath the footing. Test runs indicate that varying this parameter by an order of one or two does not significantly affect the results. An automatic load stepping scheme is used to solve the quasistatic problems (Sheng and Sloan 2001), although alternative algorithms may well be used in some problems. For example, the Newton-Raphson scheme is tested on the footing problem and gives almost identical results. The explicit stress integration scheme with automatic substepping and error control is used to solve the stresses at the integration points (Sloan et al. 2001, 2002), due to its efficiency and robustness.

In all the analyses presented in this section, the discretization of contact surfaces follows the node-to-segment approach as described in Wriggers (2002) and Sheng et al. (2006b). A number of alternative methods exist in the literature, such as the node-to-node discretization used by Katona (1983). The main advantage of the node-to-segment discretization is that it works both for small and large deformations that include large relative sliding at interfaces.

### Footing Subjected to Inclined Load and Eccentric Load

The first example analyzes a strip footing on a homogeneous soil layer. The footing is subjected to a vertical load, an inclined load or an eccentric load. The soil is modeled by an elastic-perfect-plastic Mohr–Coulomb model, while the footing is treated as an elastic material with a very high Young's modulus. Such a problem is chosen because it has either an exact solution based on plasticity theory or an approximate solution from bearing capacity theory.

The geometry of the problem and its finite-element mesh are shown in Fig. 1. Quadratic elements with eight nodes and four integration points are used for both the soil and the footing. This type of element is less accurate in predicting collapse loads than high order elements (Sloan and Randolph 1982), but works better with contact kinematics. The material properties are also given in Fig. 1, where $\phi'$=effective friction angle; $\psi'$=dilation angle;

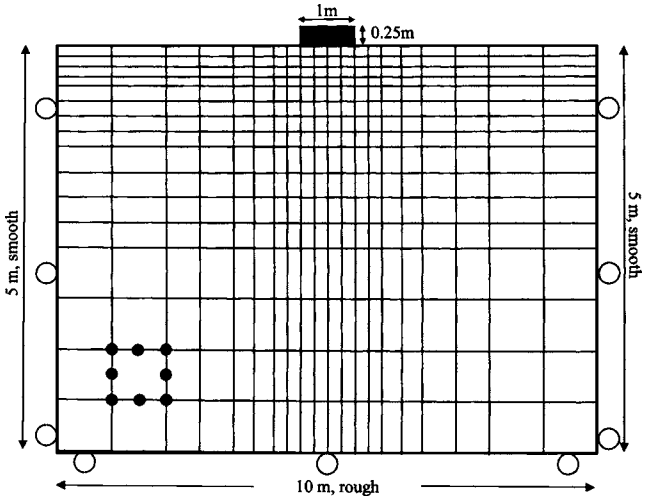


**Fig. 1.** Mesh for the strip footing (eight-noded elements with four integration points; soil properties: $\phi'=30°$, $\psi'=30°$, $c'=1$ kPa, $E=1.0\times10^5$ kPa, $\upsilon=0.3$, $\gamma=0$ or 18 kN/m$^3$ and footing properties: $B=1$ m, $E'=2\times10^8$ kPa, $\upsilon'=0.3$)

$c'$=effective cohesion; $E'$=Young' s modulus; and $\upsilon'$=Poisson's ratio. The soil is assumed to be either weightless or have $\gamma=18$ kN/m$^3$. The contact between the footing and the soil is assumed to be either smooth or have a finite friction coefficient. Initially the footing is resting on the undeformed soil. In the case of weightless soil, distributed vertical pressures or vertical displacements are prescribed at the top boundary of the footing elements. These pressures and displacements are set to sufficiently large values so that the footing collapses, and are applied typically in 20 coarse increments. For a strip footing under a uniform vertical load, there exists an exact solution for small deformation due to Prandtl and Reissner. This solution is used to verify the finite-element calculation.

When the unit weight of the soil is not zero, a step of body force loading is first performed to establish the initial stresses. Direct input of initial stresses requires an equilibrium check with prescribed displacement boundary conditions, and the resulting unbalanced forces must be carried over into subsequent time steps. Generating initial stresses by body force loading is more complicated, but ensures the stresses are always in equilibrium with the prescribed displacement boundary conditions. Once the initial stresses due to the self-weight of the soil are generated, the displacements at all nodes are reset to zero and the contact conditions are initialized by placing the footing on the soil. Distributed pressures (or vertical displacements) are then applied at the top boundary of the footing elements until collapse occurs. Approximate solutions for the collapse loads are available from bearing capacity theory (e.g., Meyerhof 1963) according to

$$q_f = c'N_c i_c + q_s N_s i_s + \tfrac{1}{2}B'\gamma N_\gamma i_\gamma$$

where $q_f$=ultimate bearing capacity; $q_s$=overburden pressure on the soil at the level of the footing base (zero in this example); $B'$=effective footing width (equal to the true footing width minus the eccentricity of the footing load); $N_c$, $N_s$, and $N_\gamma$=bearing capacity factors which are functions of the soil friction angle; and $i_c$, $i_s$, and $i_\gamma$=reduction factors due to the inclination of the footing loads. From the bearing capacity equation, we see that the self-weight of the soil should be included in order to study the effect of load eccentricity.

In Fig. 2, the footing pressures are plotted against the vertical soil displacements for a number of different loading conditions and analysis types. The footing pressures are either the applied vertical pressures or the vertical reactions at the top boundary of footing elements divided by the footing width. The vertical displacements are taken at the central soil node under the loading area. In Fig. 2(a), the strip footing is subjected to a uniform vertical load, applied in the form of prescribed displacements, and the soil is assumed to be weightless. For the smooth footing analysis using contact constraints and the UL large-deformation formulation, the predicted final footing load is 33.1 kPa, compared to the exact small-deformation solution of 30.1 kPa. In the case of a rough footing with a friction coefficient at the footing-soil interface of $\mu=0.36$ (about two-thirds of the soil friction angle), the final footing pressure is about 34.2 kPa. These final footing loads depend on the total displacements applied, because the load-displacement curves do not completely flatten out. If the same problem is analyzed using prescribed vertical displacements at the soil nodes (i.e., without the footing) and a small-deformation formulation, the predicted collapse load for the smooth footing is then 31.9 kPa and for the rough footing is 34.5 kPa. These values are, respectively, about 6 and 15% higher than the exact solution, respectively. The differences are mainly due to the mesh and the element type used in the analysis. Indeed, if 15-noded triangular elements are used for this problem, the collapse load can be predicted more accurately (Sloan et al. 2001, 2002).

Fig. 2(b) shows the load-displacement curves for the soil with self-weight. Again, we use prescribed displacements at the top nodes of the footing to predict the collapse load more accurately. The computed loads for the smooth and frictional footings ($\mu=0.36$) are quite different, and do not approach a clearly defined collapse load, due to the large deformation effects. Prescribing the displacements at the soil nodes and using a small-deformation formulation give a collapse load of 110.9 kPa for the smooth footing and 206.2 kPa for the rough footing. The conventional bearing capacity theory does not consider the effect of the friction at the footing–soil interface and the Meyerhof formula gives a collapse load of 171.1 kPa, about 54% above that for the smooth footing, but 17% below that for the frictional footing. With a friction coefficient of 0.36, the soil nodes beneath the footing experience some horizontal movement [see Fig. 3(b)]. Therefore, this type of footing cannot be considered as completely rough.

Fig. 2(c) shows the load–displacement curve for inclined loading. In this case, we have to use distributed vertical and horizontal pressures at the top boundary of the footing. The ratio between the horizontal and vertical pressures is set to 1/3, giving a resultant load which is inclined at $\theta=18.4°$ to the vertical. The friction coefficient at the soil–footing interface is set to 0.36, which ensures the footing will not have uncontrolled horizontal sliding. The soil is assumed to be weightless. The predicted collapse load in this case is 17.3 kPa, which is about 10% below the value of 19.1 kPa according to Meyerhof. The Meyerhof solution is obtained by multiplying the collapse load for purely vertical loading by the reduction factor

$$i_c = \left(1 - \frac{18.4}{90}\right)^2 = 0.63$$

Fig. 2(d) shows the load–displacement curves for loading with an eccentricity of 0.125 m. Prescribed vertical pressures are applied over the right three fourths of the top boundary of the

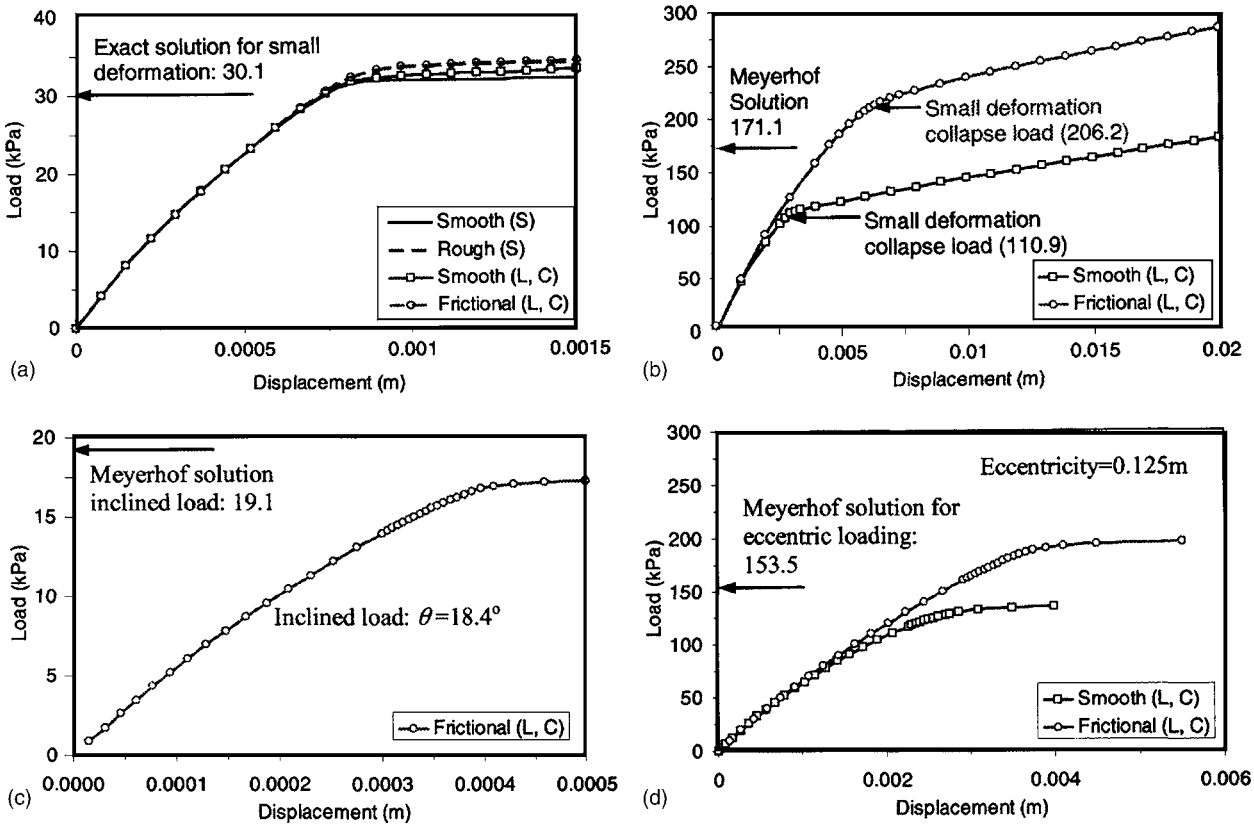


**Fig. 2.** Load–displacement curves (S=small deformation without contact; and L=large deformation; and C=contact): (a) smooth and frictional footing under vertical uniform load, weightless soil; (b) smooth and frictional footing under vertical uniform load, soil with self-weight; (c) frictional footing under inclined uniform load, weightless soil; and (d) smooth and frictional footing under eccentric load, soil with self-weight

footing. The final footing loads are 135.5 and 196.0 kPa for the smooth and frictional footing, respectively. Meyerhof suggested using the effective footing width ($B'=0.875$ m) instead of the true footing width (1 m) in bearing capacity calculations for this case. Without considering the friction at the footing-soil interface, the Meyerhof solution gives an ultimate bearing capacity of 153.5 kPa. It is again higher than the final footing load for the smooth footing, but substantially lower than that for the rough footing.

Fig. 3 shows the deformed meshes near the footing in four analyses. Only the four corner nodes of each element are used to plot the mesh, which causes some element overlap [Fig. 3(a)]. The mesh in Fig. 3(a) is for the smooth footing under a uniform vertical load where the soil has a unit weight of 18 kN/m$^3$. We see the soil nodes under the edge of the footing have experienced significant lateral movement. On each side of the footing, one soil node that is initially located underneath the foundation has moved outside it and lost contact. Such a deformation pattern indicates that imposing vertical displacements on fixed soil nodes does not really represent the actual loading condition. Fig. 3(b) shows the mesh for the uniformly loaded frictional footing on a soil with a unit weight of 18 kN/m$^3$. We see the relative movement at the soil-footing interface is not as significant as in Fig. 3(a). However, the soil nodes initially just underneath the footing edges have moved outside of the footing, indicating the frictional coefficient is not high enough to represent a completely rough footing.

Fig. 3(c) shows the mesh for the frictional footing under an inclined load. The soil is assumed to be weightless in this case. Because of the horizontal load applied to the footing, the friction coefficient for the soil–footing interface has to be larger than the ratio of the horizontal and vertical pressures, so that the footing will not have rigid body motion. This large friction coefficient also leads to a purely "stick" state at the contact interface. Therefore, the soil nodes underneath the footing experience very little horizontal movement.

Fig. 3(d) shows the mesh for the frictional footing under eccentric loading. In this case, the deformation is not symmetric

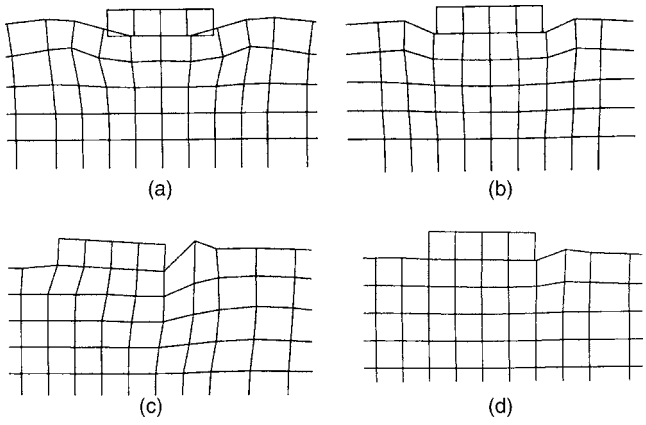


**Fig. 3.** Deformed meshes (only the four corner nodes of each eight-noded element are plotted): (a) smooth footing under vertical uniform load, soil with self-weight; (b) frictional footing under vertical uniform load, soil with self-weight; (c) frictional footing under inclined load, weightless soil; and (d) frictional footing under eccentric load, soil with self-weight

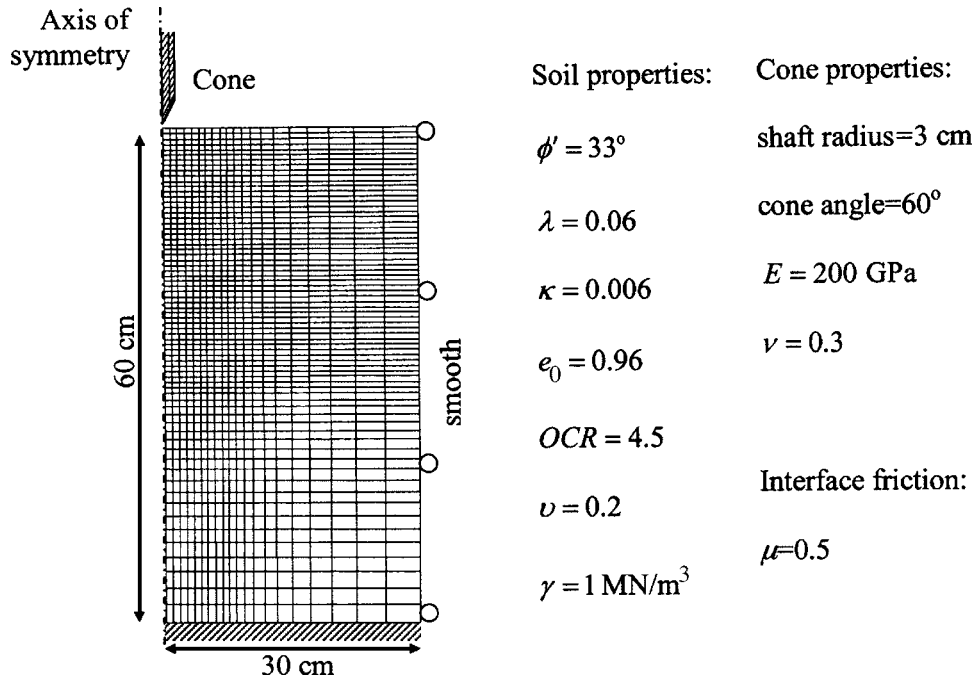


**Fig. 4.** Mesh and boundary conditions for the cone penetration test (eight-noded quadrilateral elements with four integration points)

about the center of the footing. In general, very little relative movement occurs at the soil–footing interface. However, one soil node, initially underneath the right edge of the footing, has just moved outside it and lost contact.

From this footing example, we see that incorporating contact mechanics into a finite-element formulation enables us to analyze geotechnical problems that are otherwise difficult to model. Indeed, it would be of practical interest to conduct a systematic study of footings under eccentric and inclined loading, so as to produce approximate equations or design charts for the associated bearing capacity.

### *Cone Penetration Test*

Although significant advances have been made in computational geomechanics over the last two or three decades, modeling the cone penetration test and pile driving remains a real challenge. Such modeling is important because it can improve our understanding of the physical processes involved, which in turn can lead to better interpretation of cone penetration tests and more accurate estimation of pile capacity. The two processes are so similar that the results from cone penetration tests are often used to estimate pile capacity in geotechnical practice.

Sheng et al. (1996, 1997, 2005) and Huang et al. (2004) have used the contact modeling capacity of the commercial finite-element code ABAQUS to simulate cone penetration tests and pile installation. Due to the strong nonlinearities caused by frictional contact, large deformation and elastoplasticity, obtaining convergence to a stable solution is a major challenge. This often leads to very small time steps and a very fine mesh, and hence results in extremely slow analyses. For example, using ABAQUS, a successful analysis of the penetration of a pile from the ground surface to depth of 10 radii typically requires about 100 h of computing time on a Pentium IV PC. Here, a cone penetration test is modeled on an IBM ThinkPad laptop with a Pentium M processor and takes about 2 hours to complete the penetration process from the ground surface to a depth of 10 radii of the shaft.

The mesh for the cone penetration test is shown in Fig. 4. Quadrilateral axisymmetric elements with eight nodes and four integration points are used for both the soil and the cone. The soil is modeled by the modified Cam clay model, while the cone is treated as an elastic material with a Young's modulus of 200 GPa. The soil and cone properties are given in Fig. 4, where $\lambda$=slope of the normal compression line; $\kappa$=slope of the unloading–reloading line; $e_0$=initial void ratio when the soil is under its own weight, and OCR=overconsolidation ratio.

Note that the soil column is only 60 cm in height, but the unit weight of the soil is 1 $\mathrm{MN/m^3}$ (about 50 times the real value). Therefore, a penetration depth of 1 cm in this example represents a depth of about 50 cm in a real situation. Such a setup is chosen to save computational time. Contact between the cone and soil is assumed to be frictional with $\mu$=0.5.

The cone is initially located above the ground surface. Gravity loading is first applied to the soil to establish the initial in situ stress states prior to the cone penetration. Once the initial stresses are established, the nodal displacements are set to zero, and the void ratio of the soil is set to the given value of $e_0$. The initial yield surface locations at the integration points are determined by the given OCR and the initial stress states. The cone is then pushed into the soil to the desired depth by prescribing the displacement at the top of the cone. As the soil is modeled as rate-independent material, the velocity of penetration is not of concern in the analysis.

Fig. 5 shows the deformed mesh at two penetration depths. It can be seen that the soil near the shaft is pushed sidewards and downwards, whereas elements near the ground surface are also pushed upwards. In the radial direction, the width of the first column of elements near the shaft has been reduced significantly, but the third column of elements is only slightly compressed. This means that most of the radial (sidewards) compression in the soil occurs within a horizontal distance of one shaft radius. In the vertical direction, the elements directly below the cone tip are clearly compressed, whereas the elements above the level of the

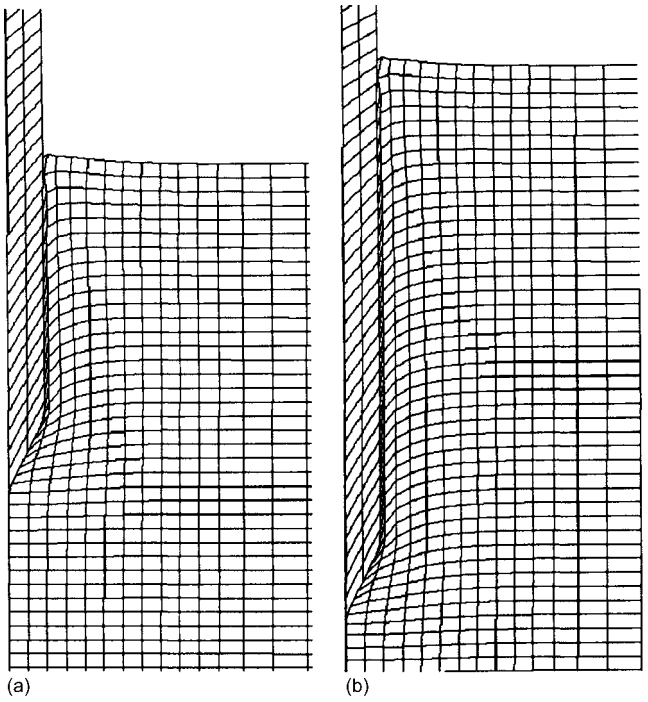


**Fig. 5.** Deformed mesh during cone penetration [(a) cone depth 14.4 cm; (b) 24.0 cm]

cone base are not significantly deformed. Except for a couple of rows of elements near the ground surface, the thickness of most element rows above the level of the cone remains relatively constant, even though the elements near the shaft have been sheared downwards. This pattern of deformation suggests that the soil undergoes vertically unloading once the cone has moved below its level. It can also be noted that the soil elements below and around the cone are not badly distorted, even though the deformations and sliding at the soil–cone interface are very large.

The computed cone resistances are depicted in Fig. 6. The computed total resistance is the sum of the vertical force due to the contact pressure and the vertical force due to the frictional stress at the interface, whereas the shaft resistance is taken as the vertical force due to the frictional stress at the interface only. The difference between the total resistance and the shaft resistance divided by the projected area of the cone (28.3 $cm^2$) gives the so-called cone resistance (MPa). The so-called sleeve

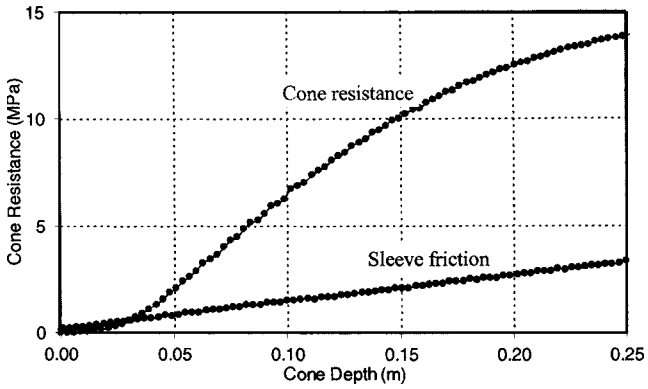


**Fig. 6.** Computed cone resistance and sleeve friction during cone penetration

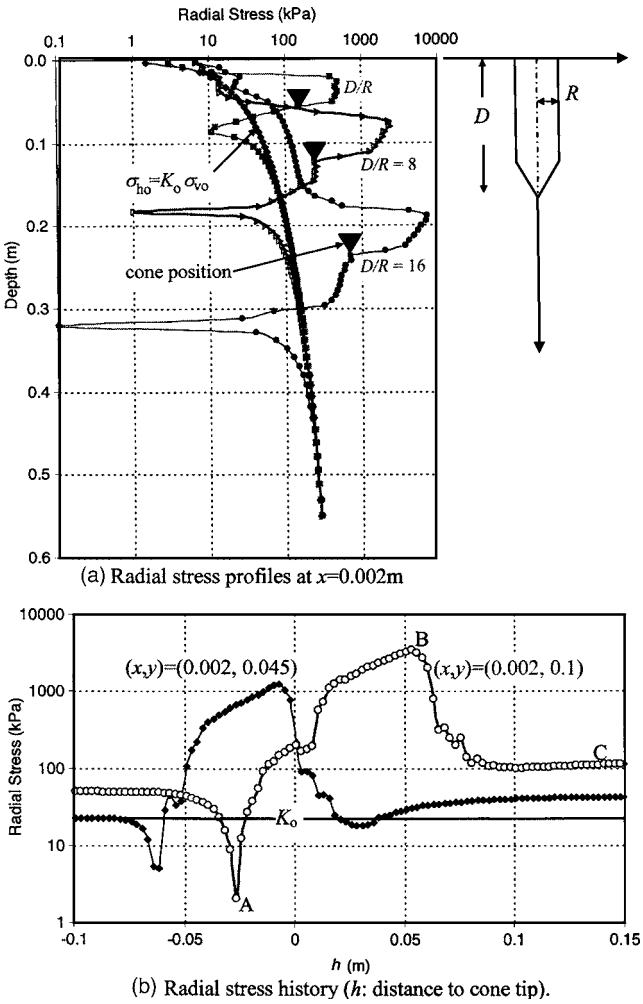


**Fig. 7.** Changes of radial stress due to cone penetration

friction is the shaft resistance divided by the total shaft surface area. The predicted patterns of the cone resistance and sleeve friction in Fig. 6 are reasonable (Lunne et al. 2001), though it is difficult to verify the values quantitatively. The relative magnitudes of the sleeve friction to the cone resistance in Fig. 6 give a friction ratio, which seems to be higher than the typical values observed during cone penetration tests. This friction ratio naturally depends very much on the interfacial friction coefficient used in the analysis. Note that the cone depth of 0.25 m in Fig. 6 would correspond to an actual depth of 12.5 m if the unit weight of the soil were set to 20 $kN/m^3$. In geotechnical engineering, the cone resistance is widely used to evaluate various strength and deformation parameters of soils. Obviously, a sensitivity analysis using the numerical method can generate correlations between the cone resistance and specific soil parameters.

During pile installation, it is often observed that the radial stress and the shaft friction experience a sharp decrease behind the pile tip. This response is referred to as "friction fatigue" by Heerema (1980) or the "$h/R$ effect" by Jardine and Chow (1996), with $h$ being the distance between the pile tip and a given point in the soil and $R$ being the radius of the pile shaft. In Fig. 7(a), the radial stresses for three different penetration/radius ratios ($D/R$) are plotted against depth and compared with the initial radial stresses. All the curves display a sharp increase in the radial stress just above the cone and a zone of small radial stress (smaller than the initial $K_0$ radial stress) at some distance below the cone tip.

For example, for $D/R=8$, the radial stress at the depth of 0.04 m (about one shaft diameter above the cone) is actually smaller than the initial $K_0$ radial stress. It increases from about 14 kPa at 0.04 m to about 2,000 kPa at 0.08 m (about half a shaft diameter above the cone). Again, the radial stress remains relatively high along the cone length, and then drops dramatically at the cone tip to about 200 kPa. It remains relatively constant for a depth of about one shaft diameter below the cone tip, and then drops further to a minimum of 1 kPa at a depth of 0.18 m (about two shaft diameters below the cone tip). The minimum radial stress below the cone tip is much less than the initial $K_0$ stress, indicating an unloading in the radial direction. The radial stress recovers to the $K_0$ value at a depth of about 4 to 5 shaft diameters below the cone tip. The curves for $D/R=4$ and $D/R=16$ basically follow the same pattern as that for $D/R=8$. Fig. 7(b) plots the radial stress variation with respect to the cone tip position. As the cone tip moves closer to and passes an observation point in the soil, the radial stress at the point first decreases to a minimum value at point A, then increases to a very high value at point A, and finally decreases again to a residual value (point C) somewhat above the initial $K_0$ value. With the modified Cam clay model used to represent the soil behavior, the large stress increase from point A to B in Fig. 7(b) is accompanied by densification of the soil (strain hardening), and the stress decrease from point B to C is accompanied by dilation or straining softening. The so-called $h/R$ effect or the friction fatigue occurs during the strain softening phase.

This example shows that the finite-element contact method can simulate the entire penetration process, from the ground surface to a desired depth. Such a process, which cannot be rigorously simulated otherwise, resolves the long-standing difficulty of estimating the effect of stress changes that accompany pile installation (Randolph et al. 1979; Bond and Jardine 1991; O'Neill 2001; White 2002). These stress changes significantly affect the capacity of the pile foundation, but are extremely difficult to measure in experiments. With accurate and robust numerical algorithms for modeling contact constraints, it is possible to take into account these stress changes when predicting pile load capacity.

## Conclusions

This paper demonstrates the application of computational contact mechanics in geotechnical engineering. It presents a general formulation for problems involving frictional contact and a general description of the associated numerical algorithms. A number of classic geotechnical problems are analyzed using contact constraints. Some key conclusions drawn from this study are:

1. Soil-structure interaction that involves large deformation and surface separation and re-closure is in general better represented by frictional contact than prescribed boundary conditions or joint elements.
2. With appropriate numerical algorithms, the finite-element method can provide accurate and robust solutions to problems involving frictional contact. These algorithms include (1) numerical treatment of contact constraints; (2) solution methods for the weak forms of the global equilibrium equation including contact contributions; and (3) solution methods for the incremental stress–strain relations for the interface.
3. In the example of the strip footing, it is confirmed that the plasticity solution by Prandtl and Reissner for a weightless soil cannot be easily extended to soils with self-weight. The bearing capacity of footings on soils with self-weight depends on the smoothness of the footing–soil contact, which is not reflected in some common bearing capacity theories. The Meyerhof formula for ultimate bearing capacity under inclined loading agrees relatively well with the numerical prediction, with the former being 10% larger.
4. The cone penetration example demonstrates that it is possible to use contact mechanics to simulate the entire penetration process from the ground surface to a desired depth. Such simulation is important for better interpretation of cone penetration tests and for accurate estimation of pile capacity.

## References


Abbo, A. J., and Sloan, S. W. (1996). "An automatic load stepping algorithm with error control." *Int. J. Numer. Methods Eng.*, 39(10), 1737–1759.

Barber, J. R., and Ciavarella, M. (2000). "Contact mechanics." *Int. J. Solids Struct.*, 37(1), 29–43.

Bond, A. J., and Jardine, R. J. (1991). "Effects of installing displacement piles in a high OCR clay." *Geotechnique*, 41(3), 341–363.

Christensen, P. W., Klarbring, A., Pang, J. S., and Stromberg, N. (1998). "Formulation and comparison of algorithms for frictional contact problems." *Int. J. Numer. Methods Eng.*, 42(1), 145–173.

Desai, C. S., and Ma, Y. (1992). "Modeling of joints and interfaces using the disturbed-state concept." *Int. J. Numer. Analyt. Meth. Geomech.*, 16(9), 623–653.

Desai, C. S., Zaman, M. M., Lightner, J. G., and Siriwardena, H. J. (1984). "Thin-layer elements for interfaces and joints." *Int. J. Numer. Analyt. Meth. Geomech.*, 8(1), 19–43.

Goodman, R., Taylor, R. L., and Brekke, T. L. (1968). "A model for the mechanics of jointed rock." *J. Soil Mech. and Found. Div.*, 94(3), 637–659.

Heerema, E. P. (1980). "Predicting pile driveability: Heather as an illustration of frictional fatigue theory." *Ground Eng.*, 13(1), 15–37.

Huang, W., Sheng, D., Sloan, S. W., and Yu, H. S. (2004). "Finite-element analysis of cone penetration in cohesionless soil." *Comput. Geotech.*, 31(7), 517–528.

Jardine, R. J., and Chow, F. C. (1996). "New design methods for offshore piles." *MTD publication no. 96/103*, Marine Technology Directorate, London.

Katona, M. G. (1983). "A simple contact-friction interface element with applications to buried culverts." *Int. J. Numer. Analyt. Meth. Geomech.*, 7(5), 371–384.

Leong, E. C., and Randolph, M. F. (1992). "A model for rock interfacial behaviour." *Public Contract Law J.*, 25(3), 187–206.

Liu, W. N., Meschke, G., and Mang, H. A. (2003). "Algorithmic stabilization of FE analysis of 2D frictional contact problems with large slip." *Comput. Methods Appl. Mech. Eng.*, 192(18), 2099–2124.

Liyanapathiranna, D. S., Deeks, A. J., and Randolph, M. F. (2000). "Numerical modeling of large deformations associated with driving of open-ended piles." *Int. J. Numer. Analyt. Meth. Geomech.*, 24(17), 1079–1101.

Lunne, T., Robertson, P. K., and Powell, J. J. M. (2001). *Cone penetration testing in geotechnical practice*, Spon Press, Taylor and Francis Group, New York.

Mabsout, M. E., Reese, L. C., and Tassoulas, J. L. (1995). "Study of pile driving by finite-element method." *J. Geotech. Engrg.*, 121(7), 535–543.

Meyerhof, G. G. (1963). "Some recent research on the bearing capacity of foundations." *Can. Geotech. J.*, 1(1), 16–26.

Nazem, M., Sheng, D., and Carter, J. P. (2006). "Stress integration and mesh refinement for large deformations in geomechanics." *Int. J. Numer. Methods Eng.*, 65(7), 1002–1027.

O'Neill, M. W. (2001). "Side resistance in piles and drilled shafts." *J. Geotech. Geoenviron. Eng.*, 127(1), 1–16.

Ooi, L. H., Boey, G. F., and Carter, J. P. (1987). "Finite-element analysis

of dilatant concrete rock interfaces." *Proc., 5th Conf. Australia on Finite-Element Methods*, Melbourne, Australia, 157–162.

Pietrzak, G., and Curnier, A. (1999). "Large deformation friction contact mechanics: Continuum formulation and augmented Lagrangian treatment." *Comput. Methods Appl. Mech. Eng.*, 177, 351–381.

Randolph, M. F., Carter, J. P., and Wroth, C. P. (1979). "Driven piles in clay: The effect of installation and subsequent consolidation." *Geotechnique*, 29(4), 361–393.

Rowe, R. K., and Armitage, H. H. (1987). "Theoretical solutions for axial deformation of drilled shafts in rock." *Can. Geotech. J.*, 24(1), 114–125.

Rowe, R. K., and Pells, P. J. N. (1980). "A theoretical study of pile-rock socket behaviour." *Proc., Int. Conf. on Structures and Foundations on Rock*, Sydney, Australia, Vol. 1, 253–264.

Sheng, D., Axelsson, K., and Magnusson, O. (1996). "Finite-element analysis of cone penetration tests." *Proc., XII Nordic Geotechnical Conf.*, Reykjvik, Iceland, pp. 75–86.

Sheng, D., Axelsson, K., and Magnusson, O. (1997). "Stress and strain fields around a penetrating cone." *Proc., 6th Int. Symp. on Numerical Models in Geomechanics (NUMG-VI)*, Montreal, Canada, Balkema, Rotterdam, The Netherlands, 456–465.

Sheng, D., Egenbrod, K. D., and Wriggers, P. (2005). "Finite-element analysis of pile driving using large-slip frictional contact." *Comput. Geotech.*, 32(1), 17–26.

Sheng, D., and Sloan, S. W. (2001). "Load stepping methods for critical state models." *Int. J. Numer. Methods Eng.*, 50(1), 67–93.

Sheng, D., Sloan, S. W., and Abbo, A. J. (2002). "An automatic Newton-Raphson scheme." *Int. J. Geomech.*, 2(4), 471–502.

Sheng, D., Sloan, S. W., Gens, A., and Smith, D. W. (2003). "Finite-element formulation and algorithms for unsaturated soils. Part I: Theory." *Int. J. Numer. Analyt. Meth. Geomech.*, 27(9), 745–765.

Sheng, D., Sun, D., and Matsuoka, H. (2006a). "Cantilever sheet-pile wall modelled by frictional contact." *Soils Found.*, 46(1), 29–37.

Sheng, D., Wriggers, P., and Sloan, S. W. (2006b). "Improved numerical algorithms for frictional contact in pile penetration analysis." *Comput. Geotech.*, in press.

Sloan, S. W., Abbo, A. J., and Sheng, D. (2001). "Refined explicit integration of elastoplastic models with automatic error control." *Eng. Comput.*, 18(1), 121–154.

Sloan, S. W., Abbo, A. J., and Sheng, D. (2002). "Erratum." *Eng. Comput.*, 19, 594.

Sloan, S. W., and Randolph, M. F. (1982). "Numerical prediction of collapse loads using finite-element methods." *Int. J. Numer. Analyt. Meth. Geomech.*, 6(1), 47–76.

Van den Berg, P. (1994). "Analysis of soil penetration." Ph.D. thesis, Technische Universiteit Delft, Delft, The Netherlands.

White, D. J. (2002). "An investigation into the behaviour of pressed-in piles." Ph.D. dissertation, Univ. of Cambridge, Cambridge, Mass.

Wilson, E. L. (1992). "Finite-elements for foundations, joints and fluid." *Developments in soil mechanism—IV: Advanced geotechnical analyses*, P. K. Banerjee and R. Butterfield, eds., Elsevier Applied Science, Amsterdam, The Netherlands, 319–350.

Wriggers, P. (2002). *Computational contact mechanics*, Wiley, Chichester, U.K.